

Unpaired cross-modality educed distillation (CMEDL) applied to CT lung tumor segmentation

Jue Jiang, Andreas Rimner, Joseph O. Deasy, and Harini Veeraraghavan

Abstract—Accurate and robust segmentation of lung cancers from CTs is needed to more accurately plan and deliver radiotherapy and to measure treatment response. This is particularly difficult for tumors located close to mediastinum, due to low soft-tissue contrast. Therefore, we developed a new cross-modality educed distillation (CMEDL) approach, using unpaired CT and MRI scans, whereby a teacher MRI network guides a student CT network to extract features that signal the difference between foreground and background. Our contribution eliminates two requirements of distillation methods: (i) paired image sets by using an image to image (I2I) translation and (ii) pre-training of the teacher network with a large training set by using concurrent training of all networks. Our framework uses an end-to-end trained unpaired I2I translation, teacher, and student segmentation networks. Our framework can be combined with any I2I and segmentation network. We demonstrate our framework's feasibility using 3 segmentation and 2 I2I methods. All networks were trained with 377 CT and 82 T2w MRI from different sets of patients. Ablation tests and different strategies for incorporating MRI information into CT were performed. Accuracy was measured using Dice similarity (DSC), surface Dice (sDSC), and Hausdorff distance at the 95th percentile (HD95). The CMEDL approach was significantly ($p < 0.001$) more accurate than non-CMEDL methods, quantitatively and visually. It produced the highest segmentation accuracy (sDSC of 0.83 ± 0.16 and HD95 of $5.20 \pm 6.86\text{mm}$). CMEDL was also more accurate than using either pMRI's or the combination of CT's with pMRI's for segmentation.

Index Terms—Unpaired distillation, cross-modality CT-MR learning, concurrent teacher and student training, lung tumor segmentation.

I. INTRODUCTION

A key unmet need in oncology is the automated and accurate segmentation of lung cancers from computed tomography (CT), to more accurately plan and deliver radiotherapy and to measure treatment response. CT is the standard-of-care imaging modality used for diagnosis and routine management of patients with lung cancers. However, CT lacks sufficient soft-tissue contrast [1] for robust and accurate segmentation of tumors and organs located in or abutting the mediastinum. Non-deep learning methods for segmenting tumors enclosed within the lung parenchyma [2], [3] have been improved with deep learning methods [4]–[8]. Segmentation accuracy has been further improved by using pre-processing to focus the algorithm towards only slices containing the tumor [9], as well as by extracting the lung parenchyma using thresholding [10]. Other methods used shape priors combined with information from three different views [11] and a dense combination of features from residual networks [12] for lung tumor segmentation. However, segmenting out the lung parenchyma to focus tumor segmentation does not help those tumors located within the mediastinum (as tumors themselves will be automatically removed). Although residual connections can help

with small tumors, performance is less promising for centrally located tumors [4].

A different approach to improve inference on lower contrast CTs is to leverage a different higher contrast modality, in particular magnetic resonance imaging (MRI), either to extract a pseudo MRI (pMRI) contrast that contains higher soft-tissue contrast [13], or to combine pMRI with CT (as CT has higher bony contrast) [14]. Our approach builds on these ideas where the MR information is used to guide the extraction of CT features that emphasize the difference between foreground and background structures. However, unlike in [13], [14], MRI is not used to perform the actual segmentation. We also use hint-learning [15], [16] based distillation but with unpaired CT and MR image sets, whereby a CT (or student) network "mimics" the features produced by a MRI (or teacher) segmentation network in order to extract more informative features for segmentation on CT.

Unpaired distillation has been used to solve a different problem of learning with few labeled datasets by leveraging additional data from a different modality to improve CT-based organ segmentation [17]–[19]. For example, a shared network representation matching the feature distributions across all layers using different combinations of the CT and MR images was used for cardiac and abdomen organs segmentation [17] with relatively small datasets. Similarly, pseudo CTs from MRI were used to produce additional CT training cases as well as provide shape priors from MRI for cardiac organs segmentation [18], [19].

Our approach fundamentally differs from the prior distillation learning methods in several ways. First, we use unpaired cross-modality distillation for tumor segmentation. Second, unlike in knowledge compression methods [20]–[22], both the teacher and student network are trained concurrently, obviating the need for large training sets to pre-train the teacher network. Third, our approach uses transformation into a higher-contrast MRI modality to provide "hints" to the student CT network to extract relevant features that better differentiate foreground from background. As a result, our approach, which we call cross-modality educed distillation learning (CMEDL, pronounced "C-medal") leads to more accurate segmentation than a CT only network even which is trained with a reasonably sized dataset.

Our framework consists of a cross-modality image-to-image translation (I2I) network and concurrently trained teacher (MRI) and student (CT) segmentation networks. The I2I translation network allows for training with unpaired image sets by synthesizing corresponding pMRI images for knowledge distillation. Concurrent teacher and student network training obviates the need for large datasets for pre-training the teacher network [18], [23]. Teacher network pre-training with large datasets is not even practical in our setting, because thoracic MRI is less commonly acquired than CTs.

Our contributions include:

- An unpaired cross-modality distillation CT segmentation framework that uses more informative MRI to guide the extraction of informative features from low soft-tissue contrast CT.
- An architecture independent framework that can be generally combined with any segmentation and I2I translation network. We demonstrate feasibility using three different segmentation and two different I2I networks.

This work was partially supported by the MSK Cancer Center support grant/core grant P30 CA008748 and NCI R01 CA198121.

J. Jiang, J.O. Deasy, and H. Veeraraghavan are all with the Department of Medical Physics, Memorial Sloan Kettering Cancer Center, NY (e-mail: jiangj1@mskcc.org; deasyj@mskcc.org; veerar@mskcc.org).

A. Rimner is with Department of Radiation Oncology, Memorial Sloan Kettering Cancer Center, NY (e-mail: rimnera@mskcc.org).

- A concurrent mutual distillation framework that obviates the need for large datasets for pre-training the teacher network. Importantly, we show that a teacher network trained without any expert-segmented real MRI data can still improve the accuracy over a CT only network, indicating that this approach can work even with unlabeled teacher modality datasets.
- We performed extensive analysis of accuracy under various conditions of using pMRI information and ablation experiments.

Our paper builds on our previously published work on lung tumor segmentation [24], but with considerable extensions, including the implementation of CMEDL on a deep multiple resolution residual network (MRRN) segmentation [4] and use of a variational auto-encoder for I2I translation [25]. We also provide: analysis on an enlarged test set of 609 patients (333 was used previously [4]); experiments to evaluate distillation learning without any expert-segmented data for the teacher network; accuracy evaluations using various strategies for incorporating pMRI information; evaluations of pMRI translation accuracy; the ability to separate tumor from background through unsupervised clustering using CMEDL distilled features; inter-rater robustness evaluation; and ablation tests.

II. RELATED WORKS

1) *Distillation for model compression*: Distillation learning was initially developed as an approach for knowledge compression applied to object classification [20], whereby simpler models with fewer parameters were extracted from a pre-trained high-capacity teacher network. Distillation was accomplished by regularizing a student network to mimic the probabilistic “softMax” outputs of a teacher network [20], [21] or the intermediate features in a high capacity model [15], [16], [26], [27]. Knowledge distillation has been successfully applied to object detection [26], natural image segmentation [27], and more recently for medical image analysis [22], [28], [29]. Model compression is typically meaningful when the high-capacity teacher network is computationally infeasible for real-time analysis [21]. In medical imaging, knowledge distillation using the standard network compression idea has been used for segmentation [22], [28] and MRI reconstruction [29] using the same modality. However, a key requirement of all the aforementioned knowledge distillation methods is the availability of a high-capacity teacher network, pre-trained on a large training corpus.

2) *Distillation for knowledge augmentation*: A different approach to distillation learning considers the problem of increasing knowledge without requiring a large pre-trained teacher network. The problem is then cast as collaborative learning [30], [31] where multiple weak learners solving the same task are trained collaboratively to improve robustness. Knowledge is added because the networks use different parameter initialization and extract slightly different representations. The key idea here is that increasing robustness improves accuracy. This idea has been shown to be highly effective in self-distillation tasks, where the knowledge learned by a teacher can be refined and improved through hidden self-training of “seeded” student networks with the same architectural complexity as teacher for classification tasks [32]. The computational complexity of sequential training of learners was recently addressed by using models extracted at previous iterations (as teachers) to regularize the models computed in subsequent iterations (as students) [33]. However, robustness is defined in the context of achieving consistent inference regardless of the initialization conditions. Although important, improving robustness to initial conditions does not guarantee robustness to imaging conditions.

Another aspect of adding knowledge through distillation concerns the problem of learning with limited data annotations by leveraging

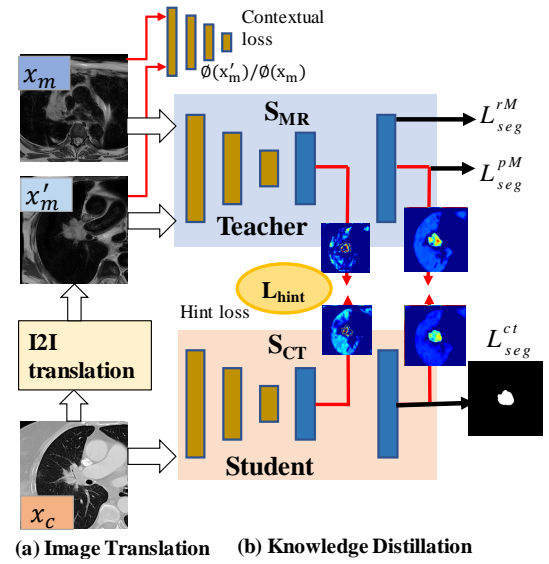


Fig. 1. Approach overview. x_c , x_m are the CT and MR images from unrelated patient sets; x'_m is the pseudo MRI (pMRI) image; x'_c is the pseudo CT image; S_{MR} is the teacher network; S_{CT} is the student CT segmentation network; Contextual, hint, generator/discriminator losses, and segmentation (L_{seg}^{rM} , L_{seg}^{pM} , L_{seg}^{ct}) losses regularize networks' training. Any unpaired I2I translation network can be used.

different sources of information [17]–[19], [34]. In this approach, distinct labeled datasets (e.g. CT and MRI), arising from different sets of patients are used to train two separate networks. Distillation consists of enforcing consistency between the networks to produce the same outputs [18], [19], matched feature distribution across few or all layers of a shared network [17], as well as cyclically consistent outputs [34] generated by the two networks.

We interpret the problem of knowledge augmentation in a completely different manner than that was used in afore-mentioned works. Concretely, we view knowledge augmentation as distilling knowledge from a more informative modality (e.g. MRI) into a less informative modality (e.g. CT) to enhance inference. In this regard, the more informative MRI is considered as the teacher, even though MRI and CT networks are trained concurrently. Our approach focuses on educing (bring forth what is hidden) the latent anatomical information shared between CT and MRI, such that the features extracted from CT are as informative as those extracted from MRI for segmentation. Importantly, no data augmentation is done from a different modality as done in other unpaired distillation methods [17]–[19]. Also as distillation only requires the student network to mimic the feature distribution of teacher network, pixel-level spatial fidelity of the synthesized pMRI is less critical than methods that use synthesized images for data augmentation.

III. METHODS

A. Cross modality educed distillation (CMEDL)

An overview of our approach is shown in Fig. 1, where two sub-networks, first for cross-modality I2I translation (i.e. CT to pMRI) (Fig. 1a), and the second (Fig. 1b) for knowledge distillation-based segmentation are used. These networks are simultaneously optimized to regularize both pMRI generation and CT, MRI segmentation. The default I2I sub-network, which uses cycleGAN [35] consists of two generators ($G_{C \rightarrow M}$ and $G_{M \rightarrow C}$) for CT to MRI and MRI to CT translation, respectively, two discriminators (D_C and D_M) and a pre-trained VGG19 [36] for calculating the contextual loss [37].

The knowledge distillation segmentation sub-network includes MRI (S_{MRI}) and CT (S_{CT}) segmentation networks.

1) Knowledge distillation segmentor: This sub-network distills pertinent information from MRI to produce tumor segmentation on CT images. For this purpose, MRI (S_{MR}) and CT (S_{CT}) segmentation networks are trained in parallel to produce tumor segmentations on these two modalities. Both networks use the same architecture to simplify hint loss computations. The MRI network is trained with both expert segmented T2w MRI ($\{x_m, y_m\} \in \{X_M, Y_M\}$) and synthesized pseudo MRI (pMRI) ($\{x_c^m, y_c^m\}$), while the CT network is trained with CT examples ($\{x_c, y_c\} \in \{X_C, Y_C\}$). Dice loss is used to optimize both networks. The loss computed using real MR data for the MR network is expressed as L_{seg}^r , the loss computed for the same network using pMR data is expressed as L_{seg}^p , and the loss for the CT network is expressed as L_{seg}^{CT} . The total segmentation loss is computed as:

$$\begin{aligned} L_{seg} &= L_{seg}^r + L_{seg}^p + L_{seg}^{CT} \\ &= \mathbb{E}_{x_m, x_c} [-\log P(y_m | S_{MR}(x_m)) \\ &\quad - \log P(y_c | S_{MR}(G_{CT \rightarrow MR}(x_c))) \\ &\quad - \log P(y_c | S_{CT}(x_c))]. \end{aligned} \quad (1)$$

The loss L_{seg}^p computed using the pMRI images helps to add more data for the teacher network, which increases the robustness of the teacher network to larger data variations.

The pMRI are used to extract features from the MR network to provide hints for the CT segmentation network. The features closest to the output have been shown to be the most correlated to the output task [38]. Hence, we matched the features extracted from the last two layers of the S_{MRI} and S_{CT} networks by minimizing the Frobenius norm:

$$L_{hint} = \sum_{i=1}^N \|\phi_{CT}^i(x_c) - \phi_{MR}^i(G_{CT \rightarrow MR}(x_c))\|_F^2, \quad (2)$$

where ϕ_{CT}^i, ϕ_{MR}^i are the i th layer features computed from the two networks, N is the total number of features.

2) Cross modality translation for unpaired distillation: This network produces pseudo MRI (pMRI) images, conditioned on the input CT images. Any cross-modality translation method can be used for this purpose. We demonstrate feasibility with two different methods.

a) CycleGAN based I2I translation: Our default implementation uses a modified cycleGAN [35] with contextual losses [37] added to better preserve spatial fidelity of structures when using unpaired image sets for training. Contextual loss is implemented by treating an image as a collection of features, where the difference between two images are computed based on all-pair feature similarities, ignoring the spatial locations. Stated differently, image matching maximizes the similarity of features computed using the generated ($f(G(X_{CT})) = g_j$) and target images ($f(X_{MR}) = m_i$) by marginalizing over all source feature similarities for every target feature. The contextual similarity is expressed as:

$$CX(g, m) = \frac{1}{N} \sum_j \max_i CX(g_j, m_i), \quad (3)$$

where, N corresponds to the number of features. The contextual similarity is computed by normalizing the inverse of cosine distances between the features in the two images as described in [37]. The contextual loss is computed as:

$$L_{cx} = -\log(CX(f(G(X_{CT})), f(X_{MR}))). \quad (4)$$

I2I network training is further stabilized using standard adversarial losses ($L_{adv} = L_{adv}^{CT} + L_{adv}^{MR}$), which maximize the likelihood that

the synthesized images (pCT, pMR) will resemble X_{CT} and X_{MRI} .

$$\begin{aligned} L_{adv}^{MRI}(G_{C \rightarrow M}, D_M, X_M, X_C) &= \mathbb{E}_{x_c \sim x_m} [\log(D_M(x_m)) \\ &\quad + \log(1 - (D_M(G_{C \rightarrow M}(x_c))) \\ L_{adv}^{CT}(G_{M \rightarrow C}, D_C, X_C, X_M) &= \mathbb{E}_{x_c \sim x_m} [\log(D_C(x_c)) \\ &\quad + \log(1 - (D_C(G_{M \rightarrow C}(x_m))) \end{aligned} \quad (5)$$

In addition, cycle consistency loss (L_{cyc}) [35] is also used to enforce cyclical consistency in the image transformations, when using the unpaired image sets, whereby, images passing through two GANs (e.g. $G_{C \rightarrow M} = G_{M \rightarrow C}(G_{C \rightarrow M}(x_c))$) will reproduce the original image (e.g. CT). This is accomplished by minimizing the pixel-to-pixel loss (through L1-norm) between the generated and original images as:

$$\begin{aligned} L_{cyc}(G_{C \rightarrow M}, G_{M \rightarrow C}, X_C, X_M) \\ = \mathbb{E}_{x_c \sim x_m} [\|G_{C \rightarrow M}(x_c) - x_c\|_1 + \|G_{M \rightarrow C}(x_m) - x_m\|_1]. \end{aligned} \quad (6)$$

The total loss is then computed as $L_{adv} + \lambda_{cyc} L_{cyc} + \lambda_{CX} L_{CX} + \lambda_{hint} L_{hint} + \lambda_{seg} (L_{seg} + L_{seg}^p)$, where λ_{cyc} , λ_{CX} , λ_{hint} and λ_{seg} are the weighting coefficients for each loss.

b) VAE based I2I translation: As an alternative I2I translation approach, we implemented the VAE using the Diverse image-to-image translation (DRIT) [39] method. This method disentangles the image into domain independent content code $E_c : x_c, x_m \rightarrow c$ and domain specific style code $E_s^c : x_c \rightarrow s_c$ for $x_c \in X_C$ and $E_s^m : x_m \rightarrow s_m$ for $x_m \in X_M$. E_c is the content encoder while E_s^c and E_s^m are the domain specific style encoders corresponding to rendering in the CT and MR domains, respectively. Domain content encoding is extracted by optimizing with a content adversarial loss:

$$\begin{aligned} L_{adv}^c &= \mathbb{E}_{x_c \sim x_m} [\log(D_c(E_c(x_c))) + (1 - \log(D_c(E_c(x_m)))) \\ &\quad + \log(D_c(E_m(x_m))) + (1 - \log(D_c(E_m(x_c))))] \end{aligned} \quad (7)$$

We also compute a content code reconstruction loss $L_{cc} : \hat{x}_j = G(E_c(x_i), E_s(x_j), d_j)$, where i is the source domain and j is the translated target domain. This is computed as:

$$L_{cc} = E[\|E_c(x_c) - E_c(\hat{x}_c)\|_1 + \|E_m(x_m) - E_m(\hat{x}_m)\|_1]. \quad (8)$$

where \hat{x}_c, \hat{x}_m are computed as $\hat{x}_c = G_c(E_c(x_c), E_s^m(x_m))$ and $\hat{x}_m = G_m(E_m(x_m), E_s^c(x_c))$, respectively. The domain specific style encodings E_s^c, E_s^m are extracted by minimizing the KL-divergence of a latent encoding computed using a conditional VAE with respect to the corresponding image domains:

$$\begin{aligned} L_{VAE} &= \mathbb{E}_{x_c \sim X_C} [D_{KL}(E_s^c(x_c) || q_c(x_c))] + \|\hat{x}_c - x_c\|_1 \\ &\quad + \mathbb{E}_{x_m \sim X_M} [D_{KL}(E_s^m(x_m) || q_m(x_m))] + \|\hat{x}_m - x_m\|_1, \end{aligned} \quad (9)$$

$q_c(x_c)$ and $q_m(x_m)$ are prior normal distributions with unit covariance $\mathcal{N}(0, I)$, and $\hat{x}_c = G_c(E_c(x_c), E_s^m(x_m))$ and $\hat{x}_m = G_m(E_m(x_m), E_s^c(x_c))$, respectively.

Image generation between the two domains is optimized using adversarial losses:

$$\begin{aligned} L_{adv} &= \mathbb{E}_{x_c \sim X_C, x_m \sim X_M} [\log(D(x_m)) + \\ &\quad 0.5 \times \log(1 - D(G_c(E_c(x_c), E_m(x_m)))) + \\ &\quad \mathbb{E}_{z \sim \mathcal{N}(0, I)} [0.5 \times \log(1 - (D(G_c(E_c(x_c), z)))] \end{aligned} \quad (10)$$

where z is sampled from $\mathcal{N}(0, I)$. In addition, latent code regression is used to regularize I2I translations.

3) Optimization: The whole network consisting of the cross-modality distillation (CT and MR segmentors) and the cross-modality adaptation (CT to MR, MR to CT generators, and discriminators) are trained jointly and end to end, where the network update alternates between the cross-modality adaptation for pMR generation and the

cross-modality distillation for CT segmentation with the following gradients, $-\Delta_{\theta_G}(L_{adv} + \lambda_{cyc}L_{cyc} + \lambda_{CX}L_{CX} + \lambda_{hint}L_{hint} + \lambda_{seg}(L_{seg} + L_{seg}^M))$, $-\Delta_{\theta_D}(L_{adv})$ and $-\Delta_{\theta_S}(L_{hint} + L_{seg} + L_{seg}^M)$.

The computed gradients when using the VAE instead of the cycleGAN are, $-\Delta_{\theta_G}(L_{adv} + \lambda_cL_{adv}^c + \lambda_{vae}L_{VAE} + \lambda_{lr}L_{lr} + \lambda_{cc}L_{cc} + \lambda_{hint}L_{hint} + \lambda_{seg}(L_{seg} + L_{seg}^M))$, $-\Delta_{\theta_D}(L_{adv})$ and $-\Delta_{\theta_S}(L_{hint} + L_{seg} + L_{seg}^M)$.

B. Networks architecture details:

a) *I2I translation network*: The default cycleGAN network was adopted from DCGAN [40], where the generators used two stride 2-convolutions, 9 residual blocks, and fractionally strided convolutions with half strides. The discriminator was implemented using the 70×70 patchGAN [41] to increase the number of evaluations for distinguishing real from fake MRI by using overlapping 70×70 image patches. Stable training was ensured by using *ReLU*, instance normalization [42] in all but the last layer, which has a *tanh* activation for image generation. Contextual loss was computed using a pre-trained VGG16 (trained on the ImageNet database). Memory requirement for computing this loss was reduced by using higher level features (after Conv7, Conv8, and Conv9 with a feature size of 64×64×256, 64×64×256 and 32×32×512). More details of these networks are in our prior work [24].

The VAE network was based on the DRIT [39] method. The content encoder E_c was implemented using a fully convolutional network and the style encoders E_s^c, E_s^m were composed of several residual blocks followed by global pooling and fully connected layers, with the output layer implemented using a reparameterization trick. Generator networks used 6 residual blocks.

b) *Segmentation networks structure*: We implemented the Unet [43], DenseFCN [44], and multiple resolution residual network (MRRN) [4] segmentation methods. The Unet [43] and DenseFCN [44] architectures are described in more detail in our prior work [24]. **The Unet** network used 4 max-pooling and 4 up-pooling layers with skip connections to concatenate the low-level and high-level features. Batch normalization (BN) and *ReLU* activation were used after the convolutional blocks. Feature distillation was done using the last two layers feature size of 128×128×64 and 256×256×64 are used to tie the features, shown as red arrow in Fig.2 (a). This network had 13.39 M parameters and 33 layers¹ of Unet.

The DenseFCN network used dense blocks with 4 layers for feature concatenation, 5 transition down for feature down-sampling, and 5 transition up blocks for feature up-sampling with a growing rate of 12. The layers from the last two blocks of DenseFCN with feature size of 128×128×228 and 256×256×192, shown as red arrow in Fig.2 (b). This resulted in 1.37 M parameters and 106 layers of DenseFCN.

Multiple resolution residual network (MRRN): The MRRN [4] is a very deep network that we previously developed for lung tumor segmentation. This network combines aspects of both densely connected [45] and residual network [46] architectures. It combines features computed at multiple image resolutions with the features computed in the deeper layers to provide higher image resolution information. Residual connections are also used between layers to increase training stability with increasing network depth. The MRRN network is composed of as many residual feature streams as the number of pooling operations used for downsampling images. The feature streams carry feature maps at specific image resolutions for combination with the deeper layer features. Four max-pooling and up-pooling are used in the encoder and decoder in MRRN.

¹layers are only counted on layers that have tunable weights

The main architectural component of the MRRN is the residual connection unit block (RCUB), which is composed of one or more serially connected residual connection units (RCU). RCU takes two inputs, feature map from the immediately preceding network layer or the output of preceding RCU and the feature map from the residual feature stream. Residual feature stream maps are processed starting from the nearest lower image resolution to the original image resolution by the successive RCUs. Each RCU consists of 3×3 convolutions, BN, and ReLU activation. The RCU has two outputs: one to connect to its successive RCU and a second feature map that is passed back to the feature stream after appropriate upsampling through residual connections. Feature distillation was implemented using features from the last two layers of size 128×128×128 and 256×256×64, as shown in by the red arrow in Fig. 2(c). This network had 25M parameters.

C. Implementation and training

All networks were implemented using the Pytorch [47] library and trained end to end on Tesla V100 with 16 GB memory and a batch size of 2. The ADAM algorithm [48] with an initial learning rate of 1e-4 was used during training for the image translation networks. The segmentation networks were trained with a learning rate of 2e-4. We set $\lambda_{adv}=1$, $\lambda_{cyc}=10$, $\lambda_{CX}=1$, $\lambda_{hint}=1$ and $\lambda_{seg}=5$ for the coefficient using CycleGAN I2I translation. When training using the DRIT VAE network, we set $L_{adv}^c = 1$, $\lambda_{vae} = 10$, $\lambda_{cc} = 10$, $\lambda_{lr} = 1$, $\lambda_{hint}=1$ and $\lambda_{seg}=5$.

Networks were trained with 58,563 2D CT image patches and 42,740 MR image patches of size 256×256 pixels enclosing the tumor and the chestwall and obtained by removing the outside part of the body through automatic thresholding from the 512×512 image. This was done by removing areas outside the body region automatically (by thresholding, followed by hole filling, and connected components extraction to identify the largest component). In addition, online data augmentation using horizontal flip, scaling, rotation, elastic deformation were applied to ensure generalizable training with sufficient data. The segmentation validation loss was monitored during the training to prevent over-fitting through early stopping strategy with a maximum training epoch of 100. Accuracy was evaluated by combining the 2D slice-wise segmentations for the whole image volume to extract 3D accuracy. The code for our approach will be made available through GitHub upon acceptance for publication.

D. Experimental comparisons

We benchmarked the accuracy of the proposed CMEDL approach against non-CMEDL CT segmentation (Unet, denseFCN, and MRRN) networks. We also evaluated the accuracy when using pMRI, which contains higher soft-tissue contrast for segmentation, similar to the approach used for pelvic organs segmentation [13]. As voxel-wise fidelity in pMRI synthesis is crucial when using pMRI for segmentation, we evaluated accuracy when using a cycleGAN [35], UNIT [25], and a cycleGAN trained concurrently with knowledge distillation in the CMEDL framework. Finally, we also evaluated the accuracy when combining the pMRI and CT images as row-wise concatenation as input to a segmentation network as was previously done for pelvic organs segmentation [14].

Weighted fusion: As there is variability in the accuracy of the generated pMR images, we also implemented a weighted concatenation approach that predicts the relative contribution of pMRI for concatenation with CT image both during training and inference. The relative contribution α was computed using a ResNet18 [46] network with 2 fully connected layers, which used the CT and

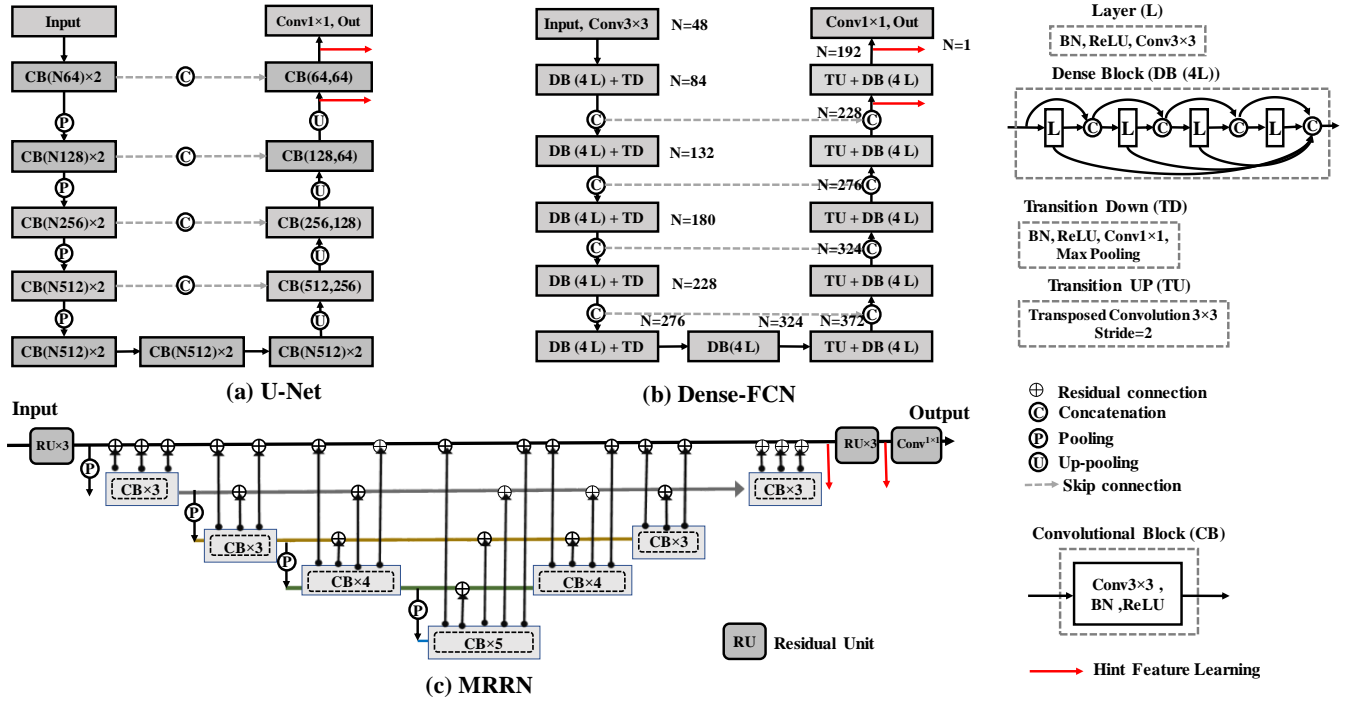


Fig. 2. The segmentation structure of U-Net [43] and DenseFCN57 [44]. The red arrow indicates that the output of these layers are used for distilling information from MR into CT. This is done by minimizing the L2-norm between the features in these layers between the two networks. The blue blocks indicate the lower layer; the green blocks indicate the middle layer; the orange blocks indicate the upper layer in U-Net. Best viewed in color.

TABLE I
OVERVIEW OF THE DIFFERENCE BETWEEN VARIOUS FUSION STRATEGIES

Method	Testing		Distillation	
	One step segmentation	No pMR synthesis	Context loss	Hint loss
CT-only	✓	✓	×	×
CMEDL	✓	✓	✓	✓
CT+pMRI	×	×	✓	×
pMRI-CMEDL	×	×	✓	✓
pMRI-UNIT	×	×	×	×
pMRI-Cycle	×	×	×	×

the corresponding pMRI as its inputs. The weighted combination is implemented as:

$$L_{seg} = \mathbb{E}_{x_c \sim X_C} [-\log S((y_c | (1 - \alpha)x_c; \alpha x_m'))] \quad (11)$$

We distinguish the above two concatenation methods as simple-CT+pMR and weighted-CT+pMR, both of which require a two-step segmentation during testing involving the cross-modality pMR synthesis followed by segmentation. A comparative description and differentiation of the various methods is in Table. I.

E. Evaluation Metrics

- **Dice similarity coefficient (DSC)** was computed by comparing the algorithm and expert-segmentation as:

$$DSC = \frac{2 \times TP}{FP + 2 \times TP + FN} \quad (12)$$

where, TP is the number of true positives, FP is the number of false positives and FN is the number of false negatives.

- **Surface DSC** is computed using the DSC of the segmented and manually labelled surface, as shown in equation 13.

$$D_{i,j}^{(\tau)} = \frac{|S_i \cap B_j^{(\tau)}| + |S_j \cap B_i^{(\tau)}|}{|S_i| + |S_j|} \quad (13)$$

Where $B_i^{(\tau)} \subset R^3$ is a border region for the surface S_i . We calculate the surface dice with the tolerance τ of 2 mm.

- **The Hausdorff distance** was computed as:

$$Hausd(P, T) = \max \left\{ \sup_{p \in S_P} \inf_{t \in S_T} (p, t), \sup_{t \in S_T} \inf_{p \in S_P} (t, p) \right\}$$

where, P and T are ground truth and segmented volumes, and p, t are points on P and T, respectively. S_P and S_T correspond to the surface of P and T, respectively. To remove the influence of noise during evaluation, we used Hausdorff Distance (95%) as recommended by Menze [49].

IV. DATASETS

We analyzed non-small cell lung cancer (NSCLC) patient datasets obtained from both internal archive and NSCLC-TCIA dataset, both consisting of patients diagnosed with lung cancers and imaged with CT imaging prior to radiation treatment. Training was done using 377 cases from the NSCLC-TCIA, while validation (N = 209 tumors from 50 patients) and testing (N = 609 tumors from 177 patients) were done on patients treated with conventional radiotherapy followed by immunotherapy at our institution. Eighty one T2w turbo spin echo MRI images sourced from 28 NSCLC patients treated with definitive intensity modulated radiation therapy at our institution and imaged every week upto 6 weeks during treatment, as described in our prior work [50] was used. Finally, we also evaluated the robustness of the approach with respect to five radiation oncologists using twenty additional cases from the open-source dataset [51].

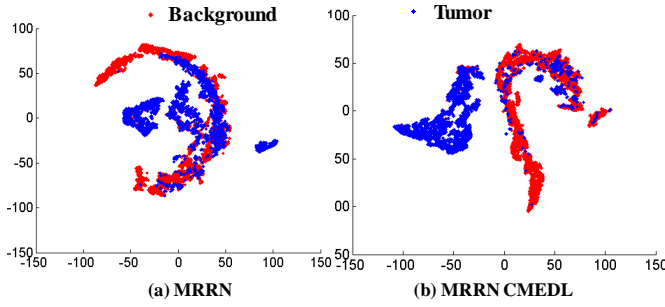


Fig. 3. T-SNE map of the CMEDL MRRN CT vs. MRRN CT features (last two layers). The T-SNE results clearly show that the CMEDL features better emphasize the difference between foreground and background.

V. EXPERIMENTS AND RESULTS

A. Network design and ablation experiments:

Ablation and network design experiments were performed using the Unet segmentation and the cycleGAN I2I network. We studied the influence of each loss, namely, the contextual loss and cycle loss for the I2I network, while the use of real MR data and pMR data for training the MR network was evaluated for the distillation network.

Design experiments evaluated the accuracy with three different segmentation architectures with and without CMEDL (cycleGAN as default I2I network), cycleGAN vs. VAE for the I2I translation (Unet segmentation), and the feature layers (low, mid vs. high) used for hint loss computation (Unet segmentation).

B. Segmentation accuracy using CMEDL

Table. II shows the segmentation accuracy on test sets computed for the various segmentation architectures with and without the CMEDL approach. The CMEDL approach was significantly more accurate than the non-CMEDL methods for all the accuracy metrics (MRRN $p < 0.001$; Unet $p < 0.001$; dense-FCN $p < 0.001$). The CMEDL-MRRN produced the best accuracy, consistent with our prior results where MRRN outperformed the Unet method [4]. Replacing the cycleGAN with VAE had little impact on accuracy with the VAE-CMEDL achieving similar accuracy as the default cycleGAN CMEDL method (Table. II).

C. Effectiveness of CMEDL extracted features for separating tumor from background

In order to understand why the CMEDL leads to improved accuracy, we performed unsupervised clustering of the features from the last two layers of the CMEDL-MRRN vs. MRRN using t-Stochastic Network Embedding (t-SNE) [52] and computed from the test dataset. Features extracted from randomly selected pixels within a 160×160 patch enclosing the tumor in each slice containing the tumor, and resulting in a total of 35,000 pixels were input to the clustering method. The number of foreground and background pixels were balanced. The clustering parameters, namely perplexity, which is related to the number of nearest neighbors was set at 60 and the number of gradient descent iterations was set to 1000. As shown in Fig. 3, the features extracted from the CMEDL-MRRN are better able to distinguish the tumor from background pixels than the features extracted from the MRRN method alone.

TABLE II

SEGMENTATION ACCURACY FOR LUNG TUMORS FROM CT USING UNET, DENSEFCN AND MRRN ON TEST SET

Method	Testing (N=609 tumors)		
	DSC	Surface DSC	HD95 mm
UNet CT only	0.69±0.20	0.73±0.21	13.44±14.69
UNet CMEDL	0.75±0.17	0.81±0.20	6.48±10.33
DenseFCN CT only	0.67±0.18	0.71±0.20	13.80±14.23
DenseFCN CMEDL	0.74±0.18	0.79±0.21	6.57±10.29
MRRN CT only	0.73±0.17	0.78±0.21	6.75±10.08
MRRN CMEDL	0.77±0.13	0.83±0.16	5.20±6.86

TABLE III

SEGMENTATION ACCURACY WITH DIFFERENT WAYS OF USING MRI. IMPLEMENTATION USED UNET.

Method (U-net)	DSC	SDSC	HD95 mm
CT only	0.69±0.20	0.73±0.21	13.44±14.69
pMRI-Cycle	0.71±0.18	0.75±0.20	12.69±13.21
pMRI-UNIT	0.71±0.17	0.76±0.22	12.47±11.25
CT+pMR	0.72±0.17	0.77±0.22	11.50±12.69
Weighted CT+pMR	0.72±0.18	0.77±0.20	11.40±12.23
pMRI-CMEDL	0.74±0.17	0.79±0.20	8.67±10.45
VAE-CMEDL	0.74±0.17	0.79±0.20	7.12±9.28
CMEDL	0.75±0.17	0.81±0.20	6.48±10.33

D. Accuracy comparison to different pMRI combination schemes

The CMEDL approach was significantly more accurate than all other pMRI combination methods, pMRI only (using either CycleGAN and UNIT) ($p < 0.001$), pMRI with CT ($p < 0.001$), and weighted pMRI with CT ($p < 0.001$). The accuracies for the various methods are shown in Table. III. We also used the pMRI produced by training using the CMEDL method (the MR network is used for segmentation instead of the default CT) for segmentation. This method was more accurate than all other pMRI methods and similarly accurate to the CMEDL approach ($p = 0.64$), indicating that mutual distillation of the MRI and CT networks benefits the teacher network also in segmentation.

Qualitative segmentation results of tumors produced by the various methods for representative test set examples are shown in Fig. 4. As shown, the CMEDL method successfully segmented the tumors, even for those tumors with unclear boundaries.

E. I2I translation accuracy

The CMEDL approach produced more accurate translation of CT to pMRI images when compared with CycleGAN and the UNIT methods. Concretely, the CMEDL method resulted in the lowest KL divergence of 0.079, compared with the CycleGAN of 0.34 and the UNIT method of 0.22. Representative pMRI images produced from CT images using the CMEDL approach are shown in Fig. 5. As shown, the boundary between tumor and normal parenchyma is clearly visualized on the pMRI images.

F. Robustness to inter-observer variations

The best performing CMEDL method, CMEDL-MRRN was used to compare against manual segmentations, by five radiation oncologists, sourced from an external institution dataset [51] consisting patients with NSCLC imaged prior to conventionally fractionated radiation treatment and imaged at a single institution. We measured the accuracy (DSC and HD95) with respect to the five raters as well as the coefficient of variation ($CV = \frac{\sigma}{\mu}$), where σ is the

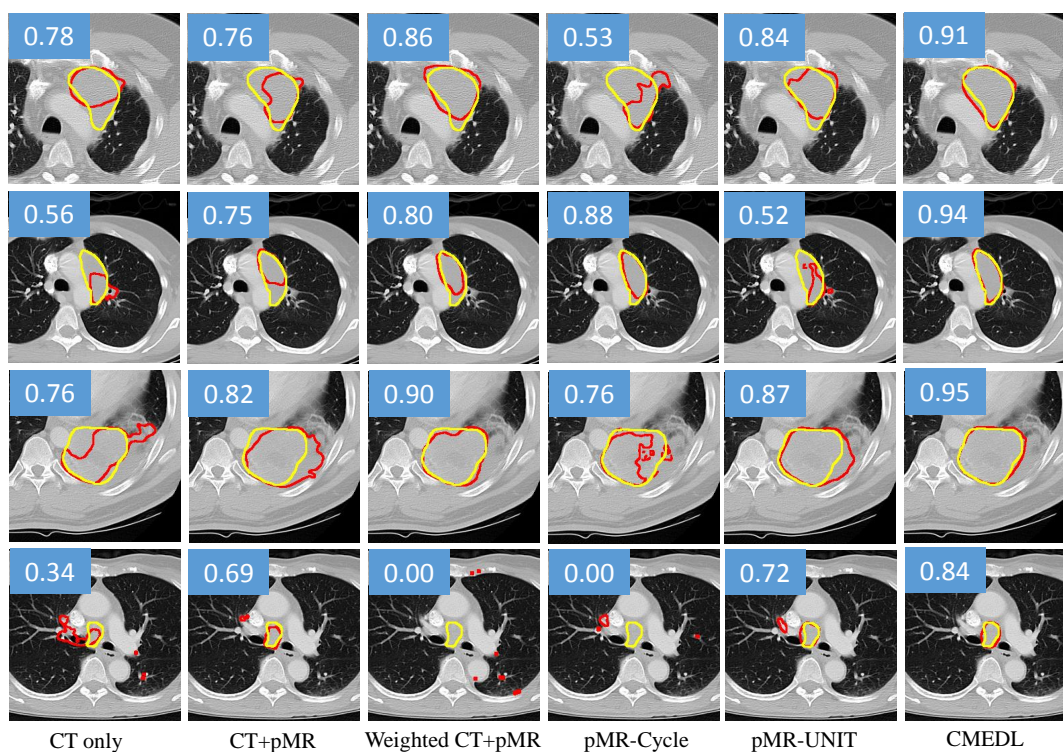


Fig. 4. Lung tumor segmentations produced by the various methods from HCT images. The Dice similarity coefficient (DSC) is also shown for these methods. Yellow contour corresponds to the expert delineation while red corresponds to the algorithm segmentation.

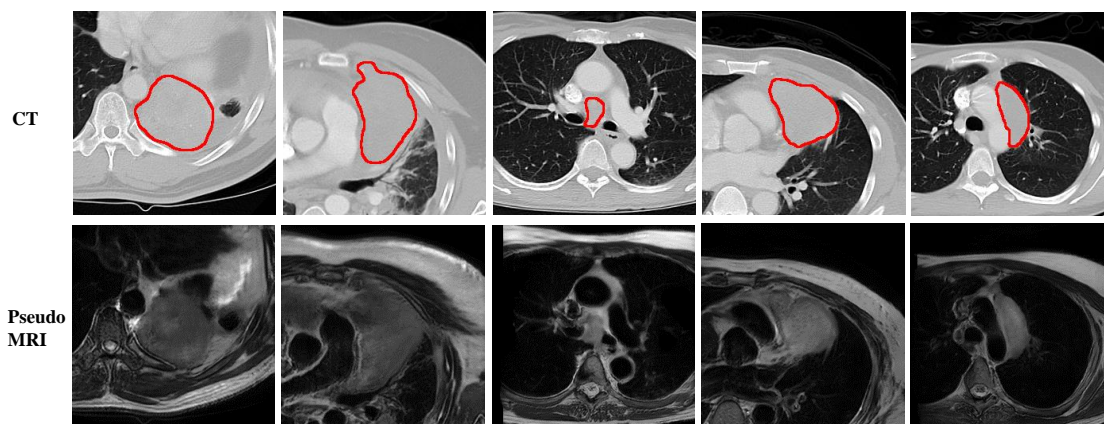


Fig. 5. Representative examples of pMRI images translated from CT images using CMEDL. The tumor region is shown by the red contour.

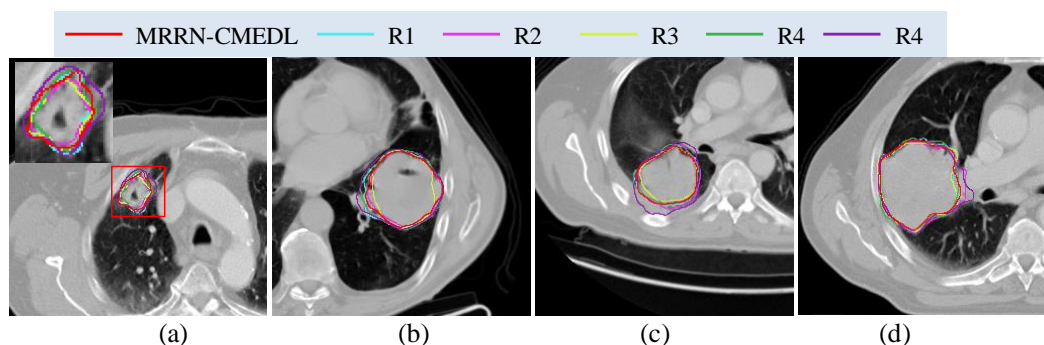


Fig. 6. Segmentation results of MRRN CMEDL compared to 5 different raters.

TABLE IV
AGREEMENT WITH RESPECT TO MULTIPLE RATERS FOR
CMEDL-MRRN.

Metric	R1	R2	R3	R4	R5	CMEDL
DSC	0.846	0.805	0.824	0.832	0.810	0.825
HD95(mm)	5.32	6.55	6.45	6.25	6.82	7.81
CV_{DSC}	0.087	0.132	0.113	0.101	0.127	0.107
CV_{HD95}	1.27	1.19	1.43	1.39	1.09	1.18

TABLE V
IMPACT OF EACH LOSS USED IN CMEDL

Setting	L_{cx}	L_{cyc}	L_{seg}^r	L_{seg}^p	DSC
1)	×	✓	✓	✓	0.72 ± 0.19
2)	✓	×	✓	✓	0.71 ± 0.19
3)	✓	✓	×	✓	0.71 ± 0.21
4)	✓	✓	✓	×	0.71 ± 0.19
5)	✓	✓	✓	✓	0.75 ± 0.17

standard deviation and μ is the population mean for both DSC and HD95 metrics using 20 patients. The results of this analysis are shown in Table. IV, where the measurements were made for each rater against all other raters and CMEDL-MRRN. CMEDL-MRRN had similar accuracy as all other raters, with a slightly higher DSC than when using R2 and R5 as reference. It also showed lower coefficient of variation than all but R5 for HD95 and all but R1 and R4 for DSC accuracy. Fig. 6 shows some representative cases with the CMEDL segmentation and the rater delineations. As seen, the algorithm segmentations are more consistent with the raters and less prone to outliers.

G. Ablation experiments

a) *Impact of various losses:* Table. V shows the impact of each loss used for training the CMEDL network. As shown, the removal of either one of pMRI (L_{seg}^p) or T2w MRI (L_{seg}^r) from training the teacher network led to a substantial reduction in accuracy. Similarly, training without either the contextual loss (L_{cx}) or the cycle loss (L_{cyc}) also led to a clear drop in accuracy, indicating that both of these losses were important to ensure reasonable spatial fidelity in the translated pMR images.

b) *Training teacher network without any expert-segmented MRI:* CMEDL training without L_{seg}^r loss is the extreme scenario where no labeled examples are available from the teacher modality. Our results show a clear drop in accuracy compared to the default CMEDL approach. However, the accuracy was still higher than the non-CMEDL approach.

c) *Impact of feature layers used for distillation:* We evaluated the how the hints from different feature layers impacted accuracy by using hints from low-level (first two convolution layers), mid-level (the bottleneck layer before upsampling), and high-level (default last and penultimate) features. As shown, hints from the low-level features led to the worst accuracy (DSC of 0.69 ± 0.21). This accuracy is comparable to the non-CMEDL Unet method, indicating that forcing similar activations of the low-level features are not meaningful. Accuracy was slightly improved when using mid-level feature hints (DSC of 0.70 ± 0.20). On the other hand, there was a clear and significant ($p < 0.001$) accuracy improvement when using the default high-level features (DSC of 0.75 ± 0.17), where only the anatomical contextual features are aligned between the two modalities compared to both low and mid-level feature hints.

H. Visualization of feature maps produced in student network of CMEDL vs. CT only network

We visualized the differences in the computed features when using CMEDL vs. non-CMEDL CT segmentation networks. Fig.7 shows example feature maps produced in the channels one to twenty four of the last layer (with size of $256 \times 256 \times 64$) of Unet (Fig.7(a)) and the features computed from the corresponding layer of a CMEDL-Unet (Fig.7(c)). For reference, the corresponding feature maps computed from pMRI using the teacher network are also shown (Fig.7(b)). As seen, the feature maps in the CT only method are less effective in differentiating the tumor regions from the background parenchyma when compared to the CMEDL approach. Furthermore, the latter network closely models the information captured in the teacher network, which we believe ultimately leads to more accurate segmentation.

VI. DISCUSSION

We developed and validated a new distillation learning method called cross-modality educed distillation (CMEDL/"C-medal") for lung tumor segmentation from CT scans. Our framework is generally applicable to other problems as well. CMEDL showed clear accuracy improvements on three different segmentation networks of varying complexity. CMEDL is also easily applied to any I2I translation method, as we demonstrated by implementing two different I2I translation methods.

A fundamental motivation of our approach is that it is applicable to general clinical image sets as it does not require paired CT and MRI scans as needed by other methods using MRI information for CT segmentation [13], [14]. This is the common clinical scenario. Also, the MRI and the I2I translation networks are only needed for training. Once trained, only the CT segmentation network is required, resulting in a computationally light-weight architecture for segmentation. Our analysis, done with the extreme condition wherein no MR labeled data was available for the teacher network, still showed performance improvements over the non-CMEDL approach. Hence, training is possible without any labeled data from the teacher modality. This is an advantage over prior works using distillation learning, which used it to increase data for robust training [17], [18]. Thus, CMEDL is more practical for medical applications. Although more data is of course better, CMEDL is effective with only a modest number of MRI's. This is an advantage over other approaches, including standard knowledge-compression based distillation methods [15], [20], [26], [27] that require the availability of a high-capacity teacher network trained on a very large dataset.

Our results showed that the educed information is most useful when used as hints through cross-modality distillation. Specifically, all approaches that used pMRI for segmentation, such as pMRI produced from CT and pMRI combined with CT were less accurate than the CMEDL approach. This indicates that matching only the feature distribution of the teacher with the student network is sufficient and more accurate than relying on the synthesized MRI (and unavoidable inaccuracies therein) for segmentation. We also verified this through unsupervised clustering of the high-level features, which clearly showed a better differentiation of tumor from background pixels when using CMEDL features. We also found that a pMRI produced through CMEDL training generated more accurate segmentations than a pMRI produced using non-CMEDL training. This result indicates that concurrent training of the student and teacher networks helped to improve the accuracy of the teacher network as well. This result is consistent with observations from prior works using concurrent training of multiple networks [30], [31] produced robust performance. We also studied the influence of distilling information from different layers of the network. Prior work by Gupta et.al [27] showed

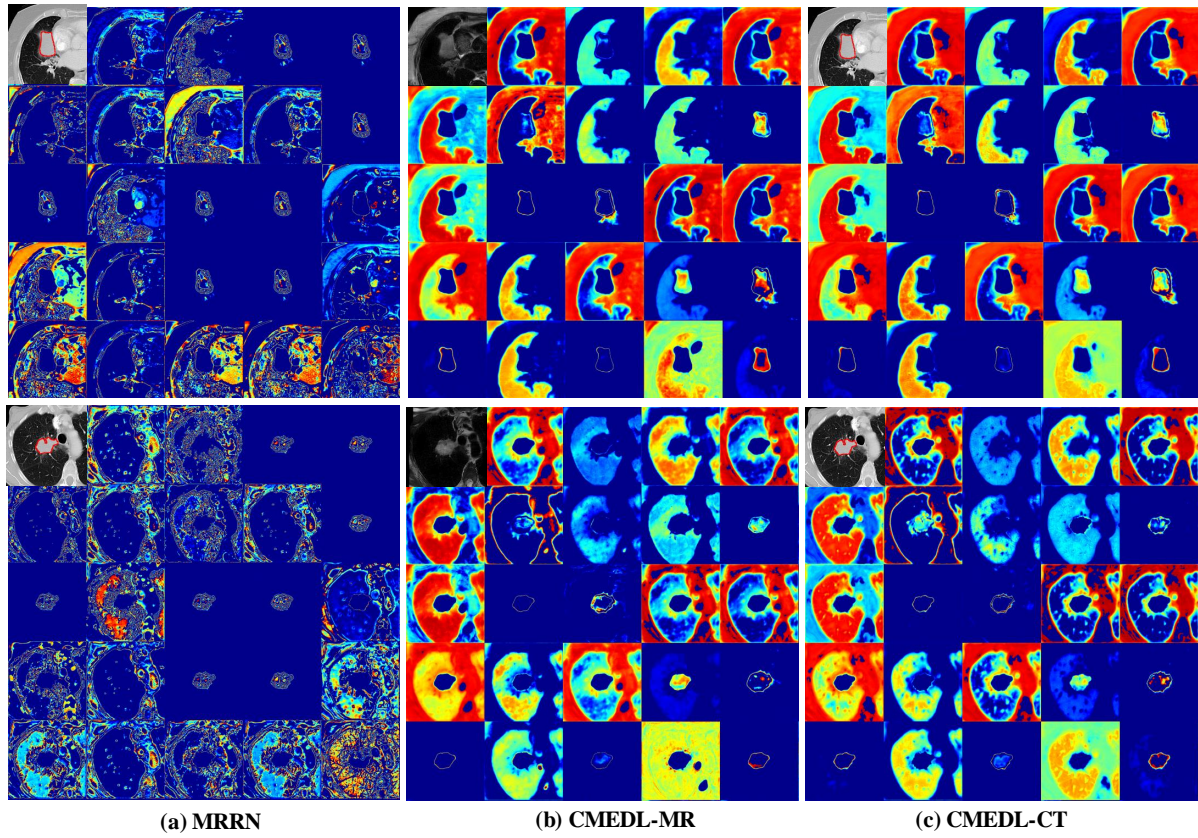


Fig. 7. The 1-24 channel feature maps from last layer of the model trained using (a) only CT images and proposed (b) CMEDL-MRI and (c) CMEDL-CT. The tumor region is enclosed in the red contour.

that distilling information from intermediate layers produced the best performance. Our results showed that the higher-level (deeper) features, which capture the high-level anatomical context, resulted in the highest accuracy. This is sensible because CT and MRI capture slightly different information about the anatomical structures but share the same anatomical context for a given disease site. Lower level (shallow) features, on the contrary, tend to emphasize low level edges and textures [38] which are not necessarily comparable between CT and MRI.

Finally, our approach showed good performance with compared to radiation oncologist segmentations, indicating the potential for this method to be used in clinical settings. One limitation of this work is the lack of validation with clinically relevant dosimetric metrics to evaluate utility for use in the clinic. This is however, work for future.

VII. CONCLUSIONS

We introduced a novel unpaired cross modality educed distillation learning approach (CMEDL) for segmenting CT image datasets by leveraging unpaired MR image sets. Our approach learns to educe the MRI information from CT by extracting informative features that emphasize the difference between foreground and background through concurrent distillation of the MR and CT networks. Our result showed clear performance improvement on multiple segmentation networks. CMEDL is a practical approach to using unpaired medical MRIs, and is a general approach to improving CT image analysis.

REFERENCES

- [1] G. A. Whitfield, P. Price, G. J. Price, and C. J. Moore, "Automated delineation of radiotherapy volumes: are we going in the right direction?" *The British journal of radiology*, vol. 86, no. 1021, pp. 20110718–20110718, 2013.
- [2] Y. Gu, V. Kumar, L. O. Hall, D. B. Goldgof, C.-Y. Li, R. Korn, C. Bendtsen, E. R. Velazquez, A. Dekker, H. Aerts et al., "Automated delineation of lung tumors from ct images using a single click ensemble segmentation approach," *Pattern recognition*, vol. 46, no. 3, pp. 692–702, 2013.
- [3] Y. Tan, L. H. Schwartz, and B. Zhao, "Segmentation of lung lesions on ct scans using watershed, active contours, and markov random field," *Medical physics*, vol. 40, no. 4, 2013.
- [4] J. Jiang, Y. Hu, C. Liu, D. Halpenny, M. D. Hellmann, J. O. Deasy, G. Mageras, and H. Veeraraghavan, "Multiple resolution residually connected feature streams for automatic lung tumor segmentation from ct images," *IEEE Transactions on Medical Imaging*, vol. 38, no. 1, pp. 134–144, Jan 2019.
- [5] B. A. Skourt, A. El Hassani, and A. Majda, "Lung ct image segmentation using deep neural networks," *Procedia Computer Science*, vol. 127, pp. 109–113, 2018.
- [6] S. Pang, A. Du, X. He, J. Díez, and M. A. Orgun, "Fast and accurate lung tumor spotting and segmentation for boundary delineation on ct slices in a coarse-to-fine framework," in *International Conference on Neural Information Processing*. Springer, 2019, pp. 589–597.
- [7] A. Tureckova, T. Turecek, Z. Kominkova Oplatkova, and A. J. Rodriguez-Sanchez, "Improving ct image tumor segmentation through deep supervision and attentional gates," *Frontiers in Robotics and AI*, vol. 7, p. 106, 2020.
- [8] X. Zhao, L. Li, W. Lu, and S. Tan, "Tumor co-segmentation in pet/ct using multi-modality fully convolutional neural network," *Physics in Medicine & Biology*, vol. 64, no. 1, p. 015011, 2018.
- [9] S. Hossain, S. Najeeb, A. Shahriyar, Z. R. Abdullah, and M. Ariful Haque, "A pipeline for lung tumor detection and segmentation from ct scans using dilated convolutional neural networks," in *ICASSP 2019 - 2019 IEEE International Conference on Acoustics, Speech and Signal Processing (ICASSP)*, 2019, pp. 1348–1352.
- [10] H. Hu, Q. Li, Y. Zhao, and Y. Zhang, "Parallel deep learning algorithms with hybrid attention mechanism for image segmentation of lung tu-

- mors,” *IEEE Transactions on Industrial Informatics*, vol. 17, no. 4, pp. 2880–2889, 2021.
- [11] S. Byun, J. Jung, H. Hong, H. Oh, and B. seog Kim, “Lung tumor segmentation using coupling-net with shape-focused prior on chest CT images of non-small cell lung cancer patients,” in *Medical Imaging 2020: Computer-Aided Diagnosis*, H. K. Hahn and M. A. Mazurowski, Eds., vol. 11314, International Society for Optics and Photonics. SPIE, 2020, pp. 598 – 603. [Online]. Available: <https://doi.org/10.1117/12.2551280>
 - [12] F. Zhang, Q. Wang, and H. Li, “Automatic segmentation of the gross target volume in non-small cell lung cancer using a modified version of resnet,” *Technology in Cancer Research & Treatment*, vol. 19, 2020.
 - [13] Y. Lei, T. Wang, S. Tian, X. Dong, A. Jani, D. Schuster, W. Curran, P. Patel, T. Liu, and X. Yang, “Male pelvic multi-organ segmentation aided by CBCT-based synthetic MRI,” *Phys Med Biol*, vol. 65, no. 3, p. 035013, 2020.
 - [14] Y. Fu, Y. Lei, T. Wang, S. Tian, P. Patel, A. Jani, W. Curran, T. Liu, and X. Yang, “Pelvic multi-organ segmentation on cone-beam ct for prostate adaptive radiotherapy,” *Med Phys*, vol. 47, no. 8, pp. 3415–3422, 2020.
 - [15] A. Romero, N. Ballas, S. E. Kahou, A. Chassang, C. Gatta, and Y. Bengio, “Fitnets: Hints for thin deep nets,” in *3rd International Conference on Learning Representations, ICLR 2015, San Diego, CA, USA, May 7-9, 2015, Conference Track Proceedings*, 2015.
 - [16] Q. Li, S. Jin, and J. Yan, “Mimicking very efficient network for object detection,” in *Proceedings of the IEEE Conference on Computer Vision and Pattern Recognition*, 2017, pp. 6356–6364.
 - [17] Q. Dou, Q. Liu, P. Ann Heng, and B. Glocker, “Unpaired multi-modal segmentation via knowledge distillation,” *IEEE Trans. Med Imaging*, vol. 39, no. 7, pp. 2415–2425, 2020.
 - [18] K. Li, L. Yu, S. Wang, and P.-A. Heng, “Towards cross-modality medical image segmentation with online mutual knowledge distillation,” *Proceedings of the AAAI Conference on Artificial Intelligence*, vol. 34, no. 01, pp. 775–783, Apr. 2020.
 - [19] K. Li, S. Wang, L. Yu, and P.-A. Heng, “Dual-teacher: Integrating intra-domain and inter-domain teachers for annotation-efficient cardiac segmentation,” in *Medical Image Computing and Computer Assisted Intervention – MICCAI 2020*. Springer International Publishing, 2020, pp. 418–427.
 - [20] G. Hinton, O. Vinyals, and J. Dean, “Distilling the knowledge in a neural network,” 2015. [Online]. Available: <http://arxiv.org/abs/1503.02531>
 - [21] C. Bucilua, R. Caruana, and A. Niculescu-Mizil, “Model compression,” in *Proceedings of the 12th ACM SIGKDD international conference on Knowledge discovery and data mining*. ACM, 2006, pp. 535–541.
 - [22] E. Kats, J. Goldberger, and H. Greenspan, “Soft labeling by distilling anatomical knowledge for improved ms lesion segmentation,” in *2019 IEEE 16th International Symposium on Biomedical Imaging (ISBI 2019)*, 2019, pp. 1563–1566.
 - [23] Z. Zhang, L. Yang, and Y. Zheng, “Translating and segmenting multimodal medical volumes with cycle- and shape-consistency generative adversarial network,” in *The IEEE Conference on Computer Vision and Pattern Recognition (CVPR)*, June 2018.
 - [24] J. Jiang, J. Hu, N. Tyagi, A. Rimmer, S. Berry, J. Deasy, and H. Veeraraghavan, “Integrating cross-modality hallucinated mri with ct to aid mediastinal lung tumor segmentation,” in *Medical Image Computing and Computer Assisted Intervention – MICCAI 2019*, D. Shen, T. Liu, T. M. Peters, L. H. Staib, C. Essert, S. Zhou, P.-T. Yap, and A. Khan, Eds. Springer International Publishing, 2019, pp. 221–229.
 - [25] Y. Li, C. Fang, J. Yang, Z. Wang, X. Lu, and M.-H. Yang, “Universal style transfer via feature transforms,” in *Advances in Neural Information Processing Systems*, 2017, pp. 386–396.
 - [26] G. Chen, W. Choi, X. Yu, T. Han, and M. Chandraker, “Learning efficient object detection models with knowledge distillation,” in *Advances in Neural Information Processing Systems*, 2017, pp. 742–751.
 - [27] S. Gupta, J. Hoffman, and J. Malik, “Cross modal distillation for supervision transfer,” in *Proceedings of the IEEE conference on computer vision and pattern recognition*, 2016, pp. 2827–2836.
 - [28] H. Wang, D. Zhang, Y. Song, S. Liu, Y. Wang, and D. Feng, “Segmenting neuronal structure in 3d optical microscope images via knowledge distillation with teacher-student network,” in *IEEE Symp Biomedical Imaging*, 2019.
 - [29] B. Murugesan, S. Vijayarangan, K. Sarveswaran, K. Ram, and M. Sivaprakasam, “KD-MRI: A knowledge distillation framework for image reconstruction and image restoration in MRI workflow,” *arXiv e-prints*, p. arXiv:2004.05319, Apr. 2020.
 - [30] G. Song and W. Chai, “Collaborative learning for deep neural networks,” in *Advances in NeurIPS*, vol. 31. Curran Associates, Inc., 2018.
 - [31] Y. Zhang, T. Xiang, T. M. Hospedales, and H. Lu, “Deep mutual learning,” in *2018 IEEE/CVF Conference on Computer Vision and Pattern Recognition*, 2018, pp. 4320–4328.
 - [32] T. Furlanello, Z. Lipton, M. Tschannen, L. Itti, and A. Anandkumar, “Born again neural networks,” in *Proceedings of the 35th International Conference on Machine Learning*, ser. Proceedings of Machine Learning Research, J. Dy and A. Krause, Eds., vol. 80. Stockholmsmässan, Stockholm Sweden: PMLR, 10–15 Jul 2018, pp. 1607–1616.
 - [33] C. Yang, L. Xie, C. Su, and A. L. Yuille, “Snapshot distillation: Teacher-student optimization in one generation,” in *2019 IEEE/CVF Conference on Computer Vision and Pattern Recognition (CVPR)*, 2019, pp. 2854–2863.
 - [34] D. He, Y. Xia, T. Qin, L. Wang, N. Yu, T.-Y. Liu, and W.-Y. Ma, “Dual learning for machine translation,” in *Advances in Neural Information Processing Systems*, vol. 29. Curran Associates, Inc., 2016.
 - [35] J.-Y. Zhu, T. Park, P. Isola, and A. Efros, “Unpaired image-to-image translation using cycle-consistent adversarial networks,” in *Intl. Conf. Computer Vision (ICCV)*. ICCV, 2017, pp. 2223–2232.
 - [36] K. Simonyan and A. Zisserman, “Very deep convolutional networks for large-scale image recognition,” *arXiv preprint arXiv:1409.1556*, 2014.
 - [37] R. Mechrez, I. Talmi, and L. Zelnik-Manor, “The contextual loss for image transformation with non-aligned data,” in *ECCV*, 2018, pp. 800–815.
 - [38] G. Lin, A. Milan, C. Shen, and I. Reid, “Refinenet: Multi-path refinement networks for high-resolution semantic segmentation,” in *Proceedings of the IEEE conference on computer vision and pattern recognition*, 2017, pp. 1925–1934.
 - [39] H.-Y. Lee, H.-Y. Tseng, J.-B. Huang, M. Singh, and M.-H. Yang, “Diverse image-to-image translation via disentangled representations,” in *Proceedings of the European conference on computer vision (ECCV)*, 2018, pp. 35–51.
 - [40] A. Radford, L. Metz, and S. Chintala, “Unsupervised representation learning with deep convolutional generative adversarial networks,” *arXiv preprint arXiv:1511.06434*, 2015.
 - [41] P. Isola, J.-Y. Zhu, T. Zhou, and A. A. Efros, “Image-to-image translation with conditional adversarial networks,” in *Proceedings of the IEEE conference on computer vision and pattern recognition*, 2017, pp. 1125–1134.
 - [42] D. Ulyanov, A. Vedaldi, and V. Lempitsky, “Improved texture networks: Maximizing quality and diversity in feed-forward stylization and texture synthesis,” in *Proceedings of the IEEE Conference on Computer Vision and Pattern Recognition*, 2017, pp. 6924–6932.
 - [43] O. Ronneberger, P. Fischer, and T. Brox, “U-net: Convolutional networks for biomedical image segmentation,” in *International Conference on Medical Image Computing and Computer-Assisted Intervention (MICCAI)*. Springer, 2015, pp. 234–241.
 - [44] S. Jégou, M. Drozdal, D. Vazquez, A. Romero, and Y. Bengio, “The one hundred layers tiramisu: Fully convolutional densenets for semantic segmentation,” in *Computer Vision and Pattern Recognition Workshops (CVPRW), 2017 IEEE Conference on*. IEEE, 2017, pp. 1175–1183.
 - [45] G. Huang, Z. Liu, L. Van Der Maaten, and K. Q. Weinberger, “Densely connected convolutional networks,” in *Proceedings of the IEEE conference on computer vision and pattern recognition*, 2017, pp. 4700–4708.
 - [46] K. He, X. Zhang, S. Ren, and J. Sun, “Deep residual learning for image recognition,” in *2016 IEEE Conference on Computer Vision and Pattern Recognition (CVPR)*, 2016, pp. 770–778.
 - [47] A. Paszke, S. Gross, S. Chintala, G. Chanan, E. Yang, Z. DeVito, Z. Lin, A. Desmaison, L. Antiga, and A. Lerer, “Automatic differentiation in pytorch,” 2017.
 - [48] D.-P. Kingma and J. Ba, “Adam: A method for stochastic optimization,” *Proceedings of the 3rd International Conference on Learning Representations (ICLR)*, 2014.
 - [49] B. H. Menze, A. Jakab, S. Bauer, J. Kalpathy-Cramer, K. Farahani, J. Kirby, Y. Burren, N. Porz, J. Slotboom, R. Wiest *et al.*, “The multimodal brain tumor image segmentation benchmark (brats),” *IEEE transactions on medical imaging*, vol. 34, no. 10, p. 1993, 2015.
 - [50] J. Jiang, Y.-C. Hu, N. Tyagi, P. Zhang, A. Rimmer, G. S. Mageras, J. O. Deasy, and H. Veeraraghavan, “Tumor-aware, adversarial domain adaptation from ct to mri for lung cancer segmentation,” in *International Conference on Medical Image Computing and Computer-Assisted Intervention*. Springer, 2018, pp. 777–785.
 - [51] P. Kalendralis, Z. Shi, A. Traverso, A. Choudhury, M. Sloep, I. Zhovannik, M. P. Starmans, D. Grittner, P. Feltens, R. Monshouwer *et al.*, “Fair-compliant clinical, radiomics and dicom metadata of rider, interobserver, lung1 and head-neck1 tcia collections,” *Medical Physics*, vol. 47, no. 11, pp. 5931–5940, 2020.

- [52] L. Van der Maaten and G. Hinton, "Visualizing data using t-sne." *Journal of machine learning research*, vol. 9, no. 11, 2008.